MATERIALS SCIENCE

Anomalous transport in high-mobility superconducting SrTiO₃ thin films

Jin Yue[1]*, Yilikal Ayino[2], Tristan K. Truttmann[1], Maria N. Gastiasoro[2]†, Eylon Persky[3], Alex Khanukov[3], Dooyong Lee[1], Laxman R. Thoutam[1]‡, Beena Kalisky[3], Rafael M. Fernandes[2], Vlad S. Pribiag[2], Bharat Jalan[1]*

The study of subtle effects on transport in semiconductors requires high-quality epitaxial structures with low defect density. Using hybrid molecular beam epitaxy (MBE), SrTiO₃ films with a low-temperature mobility exceeding 42,000 $cm^2 V^{-1} s^{-1}$ at a low carrier density of $3 \times 10^{17} cm^{-3}$ were achieved. A sudden and sharp decrease in residual resistivity accompanied by an enhancement in the superconducting transition temperature were observed across the second Lifshitz transition where the third band becomes occupied, revealing dominant intraband scattering. These films further revealed an anomalous behavior in the Hall carrier density as a consequence of the antiferrodistortive (AFD) transition and the temperature dependence of the Hall scattering factor. Using hybrid MBE growth, phenomenological modeling, temperature-dependent transport measurements, and scanning superconducting quantum interference device imaging, we provide critical insights into the important role of inter- versus intraband scattering and of AFD domain walls on normal-state and superconducting properties of SrTiO₃.

INTRODUCTION

Despite over 60 years of research, SrTiO₃ (STO) has continued to surprise researchers with new emerging behaviors (*1–4*). This is in large part due to the continuous improvement in the materials quality and the ability to make strain-engineered structures with controlled defect densities. Most recent examples include strain-enhanced superconductivity (*5, 6*) because of an interplay between ferroelectricity and superconductivity (*7–9*), and phonon thermal Hall effect (*10*).

Bulk cubic STO transforms to a tetragonal structure upon cooling below ~110 K (*11*). This is accompanied by an out-of-phase rotation of oxygen octahedra referred to as the antiferrodistortive (AFD) transition. Without an external stress/strain field, the rotational axes of these octahedra align themselves along any Cartesian axes, leading to three distinct domains. The boundaries between these domains have been shown to be charged and even ferroelectric based on several characterizations including resonant ultrasonic spectroscopy (*12*), scanning superconducting quantum interference device (SQUID) imaging (*13, 14*), piezoelectric spectroscopy measurements (*2*), scanning single-electron transistor (SET) microscopy (*15*), scanning transmission electron microscopy (*7*), and low-temperature scanning electron microscopy imaging (*16*). Domain boundaries have further been reported to modify the metal-insulator transition (*17*) and cause electrical anisotropy (*18–20*), anomalous piezoelectricity (*15*), spatial inhomogeneity in superconductivity (*21, 22*), and the softening of phonons (*23, 24*). Verma *et al.* (*25*) reported that a ~6-meV transverse optical phonon deformation potential related to the AFD transition is critical for the transport behavior between 10 and 200 K (*25*), while Zhou *et al.* (*26*) argued that the AFD soft mode has

negligible contribution to transport because of the lack of scattering phase space.

Recent experimental and theoretical studies have further renewed interest in STO because of the interplay between ferroelectricity and superconductivity. There is a substantial ongoing discussion on the presence of a quantum ferroelectric phase transition in the vicinity of the superconducting dome in STO (*3, 4, 9, 27–29*). This aspect of the behavior of STO has raised several exciting questions including the possibility of enhanced transition temperature for superconductivity at domain boundaries, which are known to be ferroelectric as discussed above. In addition, it also begs the question which role will local defects, such as dislocations, play in superconductivity. Dislocations have local stress fields around them that can potentially induce local ferroelectricity and locally enhance superconductivity (*30*). Clearly, progress on these problems requires cleaner samples with improved defect density and controlled extrinsic defects.

Using hybrid molecular beam epitaxy (MBE) (*31–33*) and through systematic control of doping, we investigate the role of AFD domain boundaries and multiband electronic structure on normal and superconducting properties in STO films. We use phenomenological modeling, temperature-dependent transport measurements, and SQUID imaging to examine their influences on the carrier density and on the superconducting transition temperature. Our results reveal that, at the vicinity of the second Lifshitz transition, intraband scattering processes dominate over interband processes, which we correlate with the observed increase in the superconducting transition temperature. Our analysis also reveals an unusual manifestation of the AFD transition on the temperature-dependent Hall scattering factor, indicating that the charge carriers display a different behavior at AFD domain walls as compared to the bulk of the sample.

RESULTS AND DISCUSSION

We begin by discussing the structural properties of STO films, which are critical to establishing a credible case for the electronic structure. Figure 1A shows representative time-dependent reflection high-energy electron diffraction (RHEED) intensity oscillations at

¹Department of Chemical Engineering and Materials Science, University of Minnesota, Minneapolis, MN 55455, USA. ²School of Physics and Astronomy, University of Minnesota, Minneapolis, MN 55455, USA. ³Department of Physics and Institute of Nanotechnology and Advanced Materials, Bar-Ilan University, Ramat Gan 5290002, Israel.
*Corresponding author. Email: yuexx129@umn.edu (J.Y.); bjalan@umn.edu (B.J.)
†Present address: ISC-CNR and Department of Physics, Sapienza University of Rome, Piazzale Aldo Moro 2, 00185, Rome, Italy.
‡Present address: Department of Electronics and Communications Engineering, SR University, Warangal Urban, Telangana 506371, India.

the onset of growth, indicating a layer-by-layer growth mode. Insets show Kikuchi bands along with surface reconstructions in post-growth RHEED images, and an atomic force microscopy (AFM) image of the same 60-nm Nd-doped STO/20-nm undoped STO film on the STO (001) substrate. These results attest to the atomically smooth film surfaces. An excellent overlap between the film and substrate peaks was observed in the wide-angle x-ray diffraction scan (Fig. 1B), yielding an out-of-plane lattice parameter (a_{OP}) of 3.905 ± 0.002 Å, identical to that of the bulk single crystal. Films with ~2% doping yielded the same a_{OP} = 3.905 ± 0.002 Å with a perfect overlap between film and substrate reflections. This observation suggests that the lattice parameter, although commonly used as an indicator for stoichiometric growth window for complex oxides (32, 34–37), should not be taken as a standalone sensitive measure of point defects in STO. To further emphasize this point, we show in Fig. 1C the temperature-dependent electron mobility of a Nd-doped STO film with a carrier density of 3×10^{17} cm^{-3}. For comparison, we also mark

on the same plot the highest low-temperature mobility values exhibited by bulk single crystalline STO (38) and pulsed-laser deposition (PLD)–grown homoepitaxial STO films (39). It can be seen that despite sharing an identical lattice parameter, our films yielded significantly higher mobility, suggesting improved defect density and lower impurity concentration.

Having established an optimum growth condition, we synthesized a series of 60-nm Nd-doped STO film/20-nm undoped STO/STO (001) by varying the doping density between 10^{19} and 10^{20} cm^{-3}, a range of carrier density where superconductivity is observed in STO. All samples showed metallic behavior between 1.8 K ≤ T ≤ 300 K with no evidence of localization behavior. At T ≤ 100 K, ρ was found to vary as T^2 in all samples (Fig. 2A); the fitting allows us to extract the intercept (ρ_0, the residual resistivity) and the coefficient (A). The value of ρ_0 as a function of room-temperature carrier density ($n_{300 K}$) is plotted in Fig. 2A, whereas the corresponding value of A is shown in fig. S1. While the physical origin of T^2 behavior is still debated (fig. S1) (40–42), an intriguing dependence of ρ_0 on $n_{300 K}$ was observed in Fig. 2B manifested by a sudden and sharp decrease at a critical density, ~ 3 to 4×10^{19} cm^{-3}. This value corresponds to the critical density for the second Lifshitz transition (43) in STO where the chemical potential (μ_C) crosses the third of the three electron-like bands of STO. It therefore raises an important question of whether the Lifshitz transition plays any role on the normal state transport.

To investigate this question, we calculated the residual resistivity as a function of band filling (n/n_c) for a toy two-band model shown in Fig. 2C (see Supplementary Materials for details). Here, n_c is the
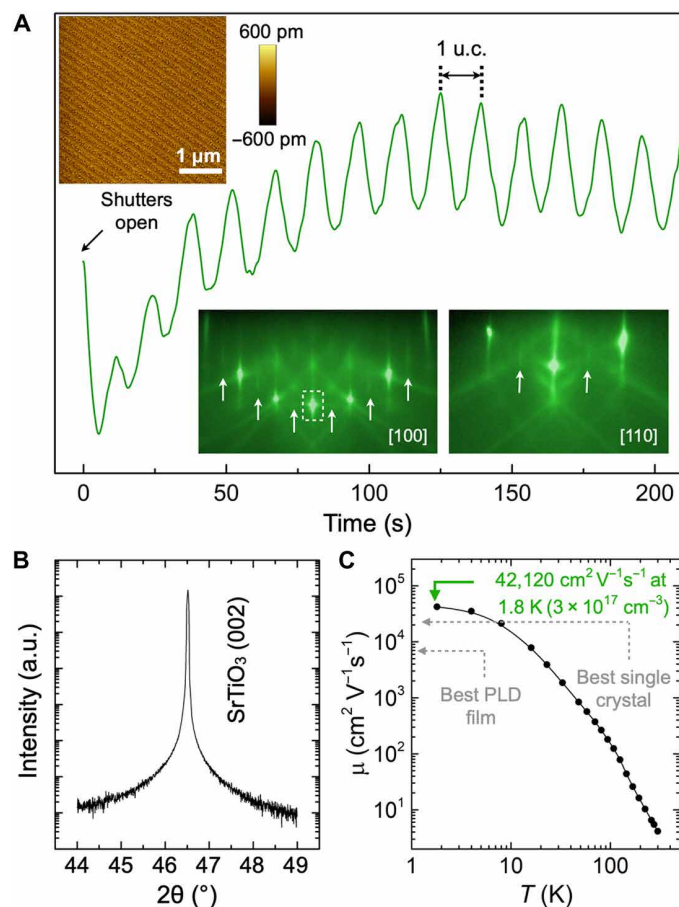

Fig. 1. Structural characterizations of Nd-doped STO films. (**A**) Time-dependent RHEED oscillation of a representative 60-nm Nd-doped STO/20-nm undoped STO film on the STO (001) substrate. The insets show the AFM image and the after-growth RHEED patterns along [100] and [110] azimuths. (**B**) High-resolution x-ray 2θ-ω coupled scan of the sample showing an epitaxial, phase pure film. (**C**) Mobility (μ) versus temperature plot for a thicker 1060-nm Nd-doped STO/20-nm undoped STO film on the STO (001) substrate with carrier density ~3×10^{17} cm^{-3} at 1.8 K with a mobility of 42,120 cm^{2}V^{-1} s^{-1}. For comparison, the highest low-temperature mobility value from the single crystal (38) and pulsed-laser deposition–grown film (39) is also depicted. a.u., arbitrary units.
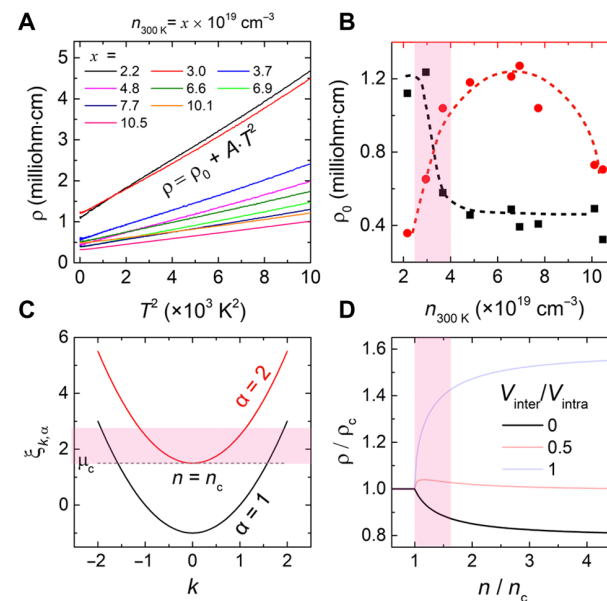

Fig. 2. Electronic transport and the calculated band structure of Nd-doped STO films. (**A**) Plot of ρ versus T^2 plots of 60-nm Nd-doped STO/20-nm undoped STO/STO (001) as a function of carrier density for T ≤ 100 K. (**B**) Residual resistivity, ρ_0 (left axis), and the superconducting transition temperature, T_c (right axis), as a function of Hall carrier density, $n_{300 K}$, illustrating a sudden and sharp decrease in ρ_0 around ~3×10^{19} cm^{-3} (marked by the pink shaded region). Black and red dashed lines are guides to the eye. (**C**) Parabolic electronic dispersions of the toy two-band system $\xi_{k,\alpha=1} = k^2/2m - \mu$ and $\xi_{k,\alpha=2} = k^2/2m + \mu_c - \mu$ with the radical momentum, k. (**D**) Calculated normalized residual resistivity ρ/ρ_c versus normalized carrier density n/n_c for various interband-to-intraband scattering strength ratios V_{inter}/V_{intra}.

critical density for the second Lifshitz transition. Because the band-splitting by tetragonality is small (~2 to 5 meV) compared to that caused by spin-orbit (SO) interactions (~12 to 30 meV) (44), we treated the lower two bands as a single one (marked by $\alpha = 1$). The third band is labeled by $\alpha = 2$ in Fig. 2C. Assuming isotropic intraband and interband scattering, we express the scattering matrix with an intraband scattering potential V_{intra} and an interband potential V_{inter}. Figure 2D shows the calculated normalized resistivity (ρ/ρ_c) as a function of n/n_c for different values of interband-to-intraband scattering potential ratio, V_{inter}/V_{intra}. Here, ρ_c refers to the residual resistivity at the critical density, n_c, corresponding to the Lifshitz transition. A remarkably similar behavior to our experimental data was observed for $V_{inter}/V_{intra} = 0$ revealing a dominant role of intraband scattering on normal-state transport across the second Lifshitz transition. To shed further light into this finding, we measured the superconducting transition temperature (T_c) in these films (fig. S2), which revealed a continuous increase in T_c across the Lifshitz transition (Fig. 2B). This result is again consistent with the prior theoretical prediction that in the absence of strong interband scattering, T_c should increase across Lifshitz transition (45). Note that this behavior is the opposite of what was seen previously at the first Lifshitz transition for much lower densities in bulk crystals, in which case T_c was found to be suppressed (43). It is perhaps worth emphasizing that unlike prior work on STO films, this is the first systematic report of a superconductivity dome in the uniformly doped STO films as thin as 60 nm, which is attributable to the lower disorder/defects in these films.

We now turn to the discussion of Hall measurements. Figure 3A shows the Hall carrier density obtained from van der Pauw (vdP) measurements ($n_{Hall} = -1/eR_H$, where R_H is the Hall coefficient) as a function of temperature for 60-nm Nd-doped STO films/20-nm undoped STO/STO (001) with different doping densities. The inset shows a linear Hall slope between $9\ T \le B \le +9\ T$ at 300 and 2.5 K. Regardless of doping density, all samples exhibited an anomalous behavior around 100 K; i.e., with increasing temperature, n_{Hall} first remains unchanged, then increases followed by a decrease, and, lastly, increases until room temperature. We also show in Fig. 3B n_{Hall} at 1.8 K as a function of n_{Hall} at 300 K for all the samples to investigate a potential correlation between carrier densities at room temperature and low temperature. Irrespective of doping density, this plot showed a linear relationship passing through origin while revealing ~12% of the room-temperature carriers seemingly disappear upon cooling to 1.8 K. This raises several questions. Why do the carriers seem to disappear upon cooling? Why is there an anomalous behavior around 100 K? Also, the linear relationship is unexpected. What role, if any, is played by the AFD, which occurs at around 100 K?

We first discuss the origin of the anomalous behavior. Conceivably, one may argue that the anomalous behavior is related to the multiband electronic conduction in STO, which makes the extraction of the carrier density from the Hall data more subtle (46). We confirmed this is not the case. Even films with single-band occupancy ($n_{Hall} = 6.5 \times 10^{17}$ cm^{-3}) yielded a similar anomalous behavior (fig. S3). Now, we consider the effect of an often overlooked, yet critical parameter—the Hall scattering factor, r_H—on the measured carrier density. r_H is defined as the ratio between the true three-dimensional (3D) carrier density (n_{3D}) and the experimentally measured Hall carrier density, n_{Hall}, i.e., $r_H = \frac{n_{3D}}{n_{Hall}}$, and is directly related to the relaxation time τ through the equation, $r_H = \frac{\langle \tau^2 \rangle}{\langle \tau \rangle^2}$ (47, 48). The value
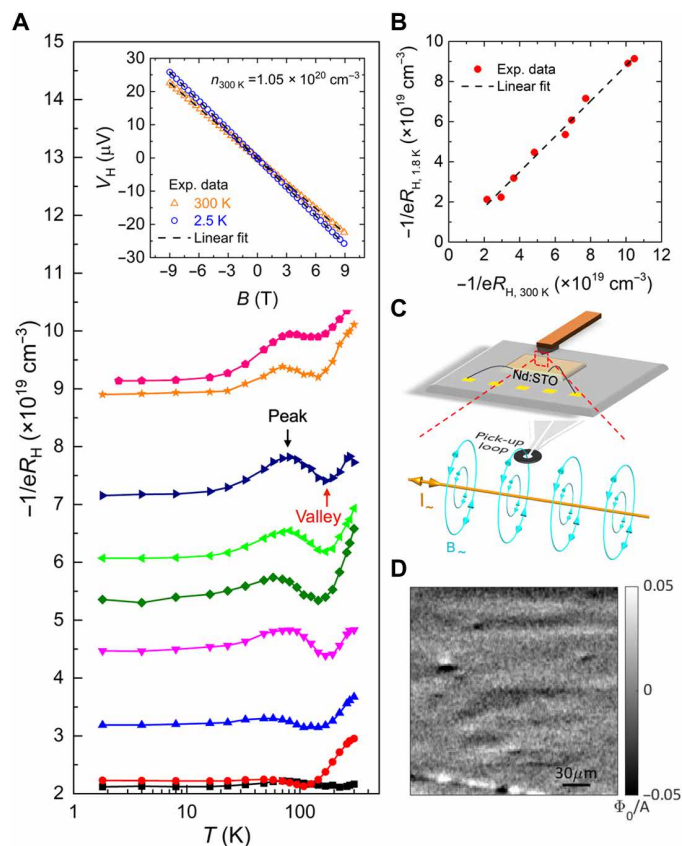

Fig. 3. Effect of AFD transition on electronic transport in doped Nd-STO films. (**A**) The Hall carrier density n_{Hall} ($-1/eR_H$) as a function of temperature for 60-nm Nd-doped STO/20-nm undoped STO/STO (001) samples for different doping densities. Inset shows linear Hall slopes at 2.5 and 300 K for a representative sample with $n_{300\,K} = 1.05 \times 10^{20}$ cm^{-3}. (**B**) n_{Hall} at 1.8 K as a function of n_{Hall} at 300 K. A black dashed line shows a linear fit to the data yielding a slope of 0.88. (**C**) A schematic of the scanning SQUID measurement setup. (**D**) Scanning SQUID image of the sample with $n_{300\,K} = 4.8 \times 10^{19}$ cm^{-3} showing the magnetic flux (ϕ_0/A) generated by the current flow at 4.5 K.

of r_H is usually close to 1, and this is perhaps why it has been assumed to be 1 in all the experimental transport studies in STO. In reality, however, the exact value of r_H depends on the band structure and scattering mechanisms. Unfortunately, there is no systematic study of r_H as a function of carrier density and temperature in STO and the only available data in literature are from ab initio calculations, as shown in fig. S4 (49). We used a polynomial interpolation to extract $1/r_H$ as a function of temperature. Because the calculated r_H is not a strong function of carrier density (49) for n_{3D} between 2×10^{19} and 2×10^{20} cm^{-3}, we used r_H corresponding to a fixed $n_{3D} = 2 \times 10^{19}$ cm^{-3} to extract temperature-dependent n_{3D} in all our samples. These results are shown in fig. S5. The anomalous behavior is not present after accounting for the temperature dependence of r_H, implying that the temperature dependence of r_H plays a major role not only in the origin of the anomalous behavior but also in determining the true carrier density. Given that the anomalous behavior of both n_{Hall} and r_H occurs near the AFD transition temperature of ~100 K, a likely mechanism for both is an AFD-driven change in the relaxation time, for instance due to the appearance of domain walls or changes in the phonon spectrum.

Although the temperature dependence of r_H accounts for the anomalous peak-and-valley pattern exhibited by n_{Hall}, a drop in carrier density as a function of decreasing temperature remains present even after correcting for this effect. One possible explanation for this effect is the emergence of AFD-induced charged/polar domain walls, which could localize some of the carriers. To investigate this hypothesis, we performed SQUID measurements. An AC current is applied through the adjacent corners of the vdP geometry as shown in Fig. 3C, and the generated magnetic flux is measured by a 0.75-μm sensing loop (pick-up loop) via a lock-in technique. By mapping the flux near the surface of the sample, a 2D map describing the local current flow distribution is generated. The scanning SQUID result of the sample with $n_{300\ K} = 4.8 \times 10^{19}$ cm^{-3} (the magenta color in Fig. 3A) at 4.5 K is shown in Fig. 3D. Some stripes and scattered dots were observed, which indicate a modulated current flow. The stripe-like modulations could be attributed to tetragonal domain patterns. These stripes did not change after a temperature cycle to 300 K, and these stripe modulations persisted to temperatures above 40 K. The low contrast could be due to the high carrier densities in our samples, which provide a high level of screening of potential steps, therefore leading to smaller current-density contrast (17, 50). As a result, it becomes very likely that not only the anomalous behavior of n_{Hall} (T) but also the drop in true density upon cooling is related to the AFD transition. However, why the dependence is linear in Fig. 3B is still unclear and may be related to an interplay between AFD and Hall scattering factor as a function of carrier density.

To further discuss the impact of AFD on the anomalous n_{Hall} behavior, we measured n_{Hall} of a representative 60-nm Nd-doped STO film/20-nm undoped STO/STO (001) sample as a function of temperature during warming and cooling. As shown in Fig. 4A, a clear difference between warming and cooling cycles was observed accompanied by the anomalous behavior. For comparison, we also performed the same measurement with the same warming/cooling rate (5 K/min) on a thicker 160-nm Nd-doped STO sample with similar n_{Hall}. In contrast, the thicker sample shows the same anomalous behavior but with no measurable differences between the cooling and warming cycles (Fig. 4B). Given the 3D carrier density is the same in both films, these results suggest that the hysteretic behavior between warming and cooling cycles are not a result of electronic transition but likely associated with the dynamic process(es) pertaining to the AFD transition resulting in carrier trapping/detrapping at domain boundaries (fig. S6). To probe the dynamic nature of the temperature-dependent n_{Hall}, we performed Hall scans at finer temperature steps on the same sample for different warming/cooling rates. Because the Hall slope is linear between ±9 T at all temperatures, a continuous temperature-dependent measurement of n_{Hall} was performed by keeping the field fixed at ±9 T. Figure 4C shows n_{Hall} as a function of temperature during warming (labeled as 1 and 3) and cooling (labeled as 2 and 4) cycles performed at two different rates, 1 and 5 K/min. Similar to Fig. 4A, a small difference in n_{Hall} was observed as a function of warming/cooling cycle. Above a critical temperature, T^*, the temperature-dependent Hall carrier density upon cooling, i.e., $[n_{Hall}\ (T)]_{cooling}$, was identical to that upon warming ($[n_{Hall}\ (T)]_{warming}$). However, at $T < T^*$, $[n_{Hall}\ (T)]_{cooling}$ remained consistently higher than $[n_{Hall}\ (T)]_{warming}$. The difference ($\Delta n_{Hall}$) between $[n_{Hall}\ (T)]_{cooling}$ and $[n_{Hall}\ (T)]_{warming}$ is plotted in Fig. 4D for two different warming/cooling rates. Figure 4D reveals that n_{Hall} strongly depends on the thermal history of the sample. A smaller T^* of ~150 K was obtained for slower warming/cooling cycle as opposed
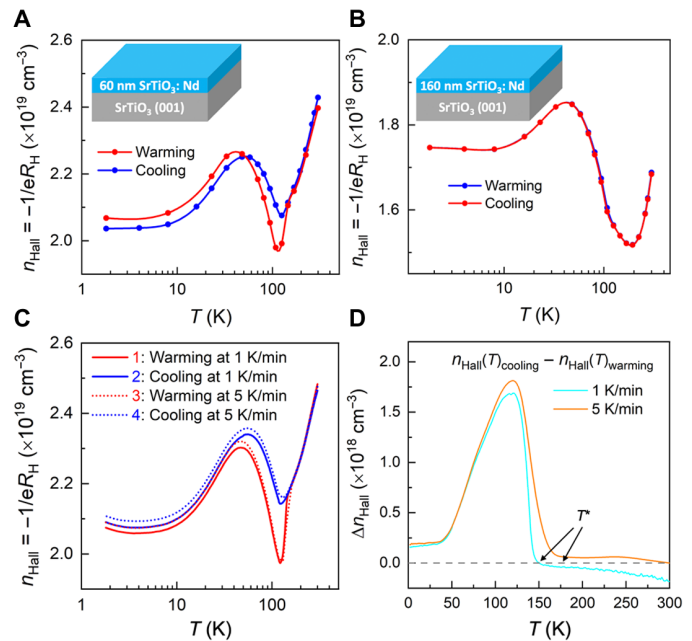

Fig. 4. Dynamic behavior across the AFD transition in Nd-doped STO films. Temperature dependence of the Hall carrier density n_{Hall} of the (**A**) 60-nm and (**B**) 160-nm Nd-doped STO sample with a similar n_{Hall} during warming and cooling cycles. (**C**) n_{Hall} and (**D**) difference of n_{Hall} between cooling and warming cycles as a function of temperature of the same 60-nm Nd-doped STO sample measured at different warming/cooling rates. T^* indicates the onset of difference in n_{Hall} between warming and cooling cycles.

to a higher $T^* = $ ~175 K for the faster warming/cooling cycle. While the peak in Δn_{Hall} occurs at identical temperature ~120 K (the expected AFD transition in doped STO) (44), the onset depends on the cooling rate, suggesting that the onset of AFD correlations begins at considerably higher temperatures. One possible explanation can be trapping/detrapping of residual oxygen vacancies, which are known to accumulate at the domain walls (51, 52). Future studies should focus on examining the normal-state transport and superconductivity at domain boundaries that may be substantially different from the global measurements.

In summary, we have investigated the electrical transport properties in hybrid MBE-grown Nd-doped STO films exhibiting low-temperature mobility exceeding 42,000 cm^{2}V^{-1} s^{-1} in the low-doped regime where not all bands are occupied. By systematically varying carrier density across the second Lifshitz transition, we found that intraband scattering dominates over interband scattering. In the normal state, this is manifested by a suppression of the residual resistivity across the second Lifshitz transition, whereas in the superconducting state, it is related to an enhancement of T_c. This behavior contrasts with that previously observed across the first Lifshitz transition, where T_c is suppressed and dominant interband scattering was proposed (45). Moreover, we showed a superconducting dome in uniformly doped STO films as thin as 60 nm. This study also provides an important connection between the AFD transition, structural dynamics, and the Hall scattering factor. In particular, it suggests that charge carriers can become more localized and experience different relaxation rates at AFD domain walls. Future experimental work should focus on a systematic study of local versus global transport.

MATERIALS AND METHODS
Film growth and characterization

All samples were grown with a hybrid MBE approach. The details of the growth method is described elsewhere (*31–33*), but a brief description is provided here. The 5 mm by 5 mm $SrTiO_3$ (001) substrates (CrysTec GmbH, Germany) were heated to 900°C (thermocouple temperature) in the hybrid MBE system (Scienta Omicron, Germany). Growth was preceded by 20 min of oxygen cleaning via 250 W RF oxygen plasma that achieves a background oxygen pressure of 5×10^{-6} torr (Mantis, UK). Strontium and neodymium were provided via thermal sublimation from an effusion cell. Strontium was supplied at 472°C to achieve a beam equivalent pressure of 4×10^{-8} torr, whereas the neodymium effusion cell temperature was varied between 780° and 980°C to control the dopant concentration. During growth, oxygen was supplied using the same oxygen plasma parameters that were used for oxygen cleaning.

RHEED was used to characterize the sample growth in situ, and AFM was used to characterize the sample surface ex situ. High-resolution XRD data were collected with a PANalytical X'Pert Pro thin film diffractometer with a Cu parabolic mirror and germanium 4-bounce monochromator. All transport data (>1.8 K) were collected in the vdP geometry in the temperature- and magnetic field–controlled environment provided by a DynaCool physical property measurement system (Quantum Design, USA). Magnetic field was swept between ±9 T. Millikelvin measurements were performed in an Oxford Triton dry dilution refrigerator equipped with homemade RC and Pi thermalizing filters mounted on the mixing chamber plate.

A buffer layer of insulating 20-nm STO was grown on each substrate before growing a doped layer to minimize the substrate surface effect. Films grown without doping were insulating with no measurable conductivity, indicating the absence of contribution of oxygen vacancies to the electrical transport. For scanning SQUID, an AC current was applied through the adjacent corners in the vdP geometry. The generated magnetic flux was measured using a 0.75-μm sensing loop (pick-up loop) via a lock-in mechanism. By mapping the flux near the surface of the sample, a 2D map describing the local current flow distribution was generated.

SUPPLEMENTARY MATERIALS
Supplementary material for this article is available at https://science.org/doi/10.1126/sciadv.abl5668

REFERENCES AND NOTES

1. K. A. Müller, W. Berlinger, E. Tosatti, Indication for a novel phase in the quantum paraelectric regime of SrTiO₃. *Z. Phys. B* **84**, 277–283 (1991).
2. E. K. H. Salje, O. Aktas, M. A. Carpenter, V. V. Laguta, J. F. Scott, Domains within domains and walls within walls: Evidence for polar domains in cryogenic SrTiO₃. *Phys. Rev. Lett.* **111**, 247603 (2013).
3. J. R. M. N. Gastiasoro, R. M. Fernandes, Superconductivity in dilute SrTiO₃: A review. *Ann. Phys.* **417**, 168107 (2020).
4. C. Collignon, X. Lin, C. W. Rischau, B. Fauqué, K. Behnia, Metallicity and superconductivity in doped strontium titanate. *Annu. Rev. Condens. Matter Phys.* **10**, 25–44 (2019).
5. R. Russell, N. Ratcliff, K. Ahadi, L. Dong, S. Stemmer, J. W. Harter, Ferroelectric enhancement of superconductivity in compressively strained SrTiO₃ films. *Phys. Rev. Mater.* **3**, 091401 (2019).
6. K. Ahadi, L. Galletti, Y. Li, S. Salmani-Rezaie, W. Wu, S. Stemmer, Enhancing superconductivity in SrTiO₃ films with strain. *Sci. Adv.* **5**, eaaw0120 (2019).
7. S. S.-Rezaie, K. Ahadi, S. Stemmer, Polar nanodomains in a ferroelectric superconductor. *Nano Lett.* **20**, 6542–6547 (2020).
8. Y. Tomioka, N. Shirakawa, K. Shibuya, I. H. Inoue, Enhanced superconductivity close to a non-magnetic quantum critical point in electron-doped strontium titanate. *Nat. Comm.* **10**, 738 (2019).
9. C. W. Rischau, X. Lin, C. P. Grams, D. Finck, S. Harms, J. Engelmayer, T. Lorenz, Y. Gallais, B. Fauqué, J. Hemberger, K. Behnia, A ferroelectric quantum phase transition inside the superconducting dome of Sr₁₋ₓCaₓTiO₃₋δ. *Nat. Phys.* **13**, 643–648 (2017).
10. X. Li, B. Fauque, Z. Zhu, K. Behnia, Phonon thermal hall effect in strontium titanate. *Phys. Rev. Lett.* **124**, 105901 (2020).
11. H. Unoki, T. Sakudo, Electron spin resonance of Fe³⁺ in SrTiO₃ with special reference to the 110°K phase transition. *J. Physical Soc. Japan* **23**, 546–552 (1967).
12. J. F. Scott, E. K. H. Salje, M. A. Carpenter, Domain wall damping and elastic softening in SrTiO₃: Evidence for polar twin walls. *Phys. Rev. Lett.* **109**, 187601 (2012).
13. Y. Frenkel, N. Haham, Y. Shperber, C. Bell, Y. Xie, Z. Chen, Y. Hikita, H. Y. Hwang, E. K. H. Salje, B. Kalisky, Imaging and tuning polarity at SrTiO₃ domain walls. *Nat. Mater.* **16**, 1203–1208 (2017).
14. B. Kalisky, E. M. Spanton, H. Noad, J. R. Kirtley, K. C. Nowack, C. Bell, H. K. Sato, M. Hosoda, Y. Xie, Y. Hikita, Locally enhanced conductivity due to the tetragonal domain structure in LaAlO₃/SrTiO₃ heterointerfaces. *Nat. Mater.* **12**, 1091–1095 (2013).
15. J. A. S. M. Honig, J. Drori, A. Joshua, E. Zeldov, S. Ilani, Local electrostatic imaging of striped domain order in LaAlO₃/SrTiO₃. *Nat. Mater.* **12**, 1112–1118 (2013).
16. H. J. H. Ma, S. Scharinger, S. W. Zeng, D. Kohlberger, M. Lange, A. Stöhr, X. R. Wang, T. Venkatesan, R. Kleiner, J. F. Scott, J. M. D. Coey, D. Koelle, Ariando, Local electrical imaging of tetragonal domains and field-induced ferroelectric twin walls in conducting SrTiO₃. *Phys. Rev. Lett.* **116**, 257601 (2016).
17. E. Persky, N. Vardi, A. Mafalda, R. V. L. Monteiro, T. C. van Thiel, H. Yoon, Y. Xie, B. Fauqué, A. D. Caviglia, H. Y. Hwang, K. Behnia, J. Ruhman, B. Kalisky, Non-universal current flow near the metal-insulator transition in an oxide interface. *Nat. Comm.* **12**, 3311 (2021).
18. N. J. Goble, R. Akrobetu, H. Zaid, S. Sucharitakul, M.-H. Berger, A. Sehirlioglu, X. P. A. Gao, Anisotropic electrical resistance in mesoscopic LaAlO₃/SrTiO₃ devices with individual domain walls. *Sci. Rep.* **7**, 44361 (2017).
19. Y. Frenkel, N. Haham, Y. Shperber, C. Bell, Y. Xie, Z. Chen, Y. Hikita, H. Y. Hwang, B. Kalisky, Anisotropic transport at the LaAlO₃/SrTiO₃ interface explained by microscopic imaging of channel-flow over SrTiO₃ domains. *ACS Appl. Mater. Interfaces* **8**, 12514–12519 (2016).
20. Q. Tao, B. Loret, B. Xu, X. Yang, C. W. Rischau, X. Lin, B. Fauqué, M. J. Verstraete, K. Behnia, Nonmonotonic anisotropy in charge conduction induced by antiferrodistortive transition in metallic SrTiO₃. *Phys. Rev. B* **94**, 035111 (2016).
21. H. Noad, P. Wittlich, J. Mannhart, K. A. Moler, Modulation of superconducting transition temperature in LaAlO₃/SrTiO₃ by SrTiO₃ structural domains. *J. Supercond. Nov. Magn.* **32**, 821–825 (2018).
22. H. Noad, E. M. Spanton, K. C. Nowack, H. Inoue, M. Kim, T. A. Merz, C. Bell, Y. Hikita, R. Xu, W. Liu, A. Vailionis, H. Y. Hwang, K. A. Moler, Variation in superconducting transition temperature due to tetragonal domains in two-dimensionally doped SrTiO₃. *Phys. Rev. B* **94**, 174516 (2016).
23. R. A. Cowley, W. J. L. Buyers, G. Dolling, Relationship of normal modes of vibration of strontium titanate and its antiferroelectric phase transition at 110°K. *Solid State Commun.* **7**, 181–184 (1969).
24. G. Shirane, Y. Yamada, Lattice-dynamical study of the 110°K phase transition in SrTiO₃. *Phys. Rev.* **177**, 858–863 (1969).
25. A. Verma, A. P. Kajdos, T. A. Cain, S. Stemmer, D. Jena, Intrinsic mobility limiting mechanisms in lanthanum-doped strontium titanate. *Phys. Rev. Lett.* **112**, 216601 (2014).
26. J. J. Zhou, O. Hellman, M. Bernardi, Electron-phonon scattering in the presence of soft modes and electron mobility in SrTiO₃ Perovskite from first principles. *Phys. Rev. Lett.* **121**, 226603 (2018).
27. P. Wölfle, A. V. Balatsky, Superconductivity at low density near a ferroelectric quantum critical point: Doped SrTiO₃. *Phys. Rev. B* **98**, 104505 (2018).
28. J. Ruhman, P. A. Lee, Superconductivity at very low density: The case of strontium titanate. *Phys. Rev. B* **94**, 224515 (2016).
29. M. N. Gastiasoro, T. V. Trevisan, R. M. Fernandes, Anisotropic superconductivity mediated by ferroelectric fluctuations in cubic systems with spin-orbit coupling. *Phys. Rev. B* **101**, 174501 (2020).
30. D. P. S. Hameed, Z. W. Anderson, A. Klein, R. J. Spieker, L. Yue, B. Das, J. Ramberger, M. Lukas, Y. Liu, M. J. Krogstad, R. Osborn, Y. Li, C. Leighton, R. M. Fernandes, M. Greven, Ferroelectric quantum criticality and enhanced superconductivity in plastically deformed strontium titanate. arXiv:2005.00514 [cond-mat.supr-con] (2020).
31. B. Jalan, R. E. Herbert, N. J. Wright, S. Stemmer, Growth of high-quality SrTiO₃ films using a hybrid molecular beam epitaxy approach. *J. Vac. Sci. Technol. A* **27**, 461–464 (2009).
32. B. Jalan, P. Moetakef, S. Stemmer, Molecular beam epitaxy of SrTiO₃ with a growth window. *Appl. Phys. Lett.* **95**, 032906 (2009).
33. J. Son, P. Moetakef, B. Jalan, O. Bierwagen, N. J. Wright, R. E. Herbert, S. Stemmer, Epitaxial SrTiO₃ films with electron mobilities exceeding 30,000 cm²V⁻¹ s⁻¹. *Nat. Mater.* **9**, 482–484 (2010).
34. A. Prakash, P. Xu, X. Wu, G. Haugstad, X. Wang, B. Jalan, Adsorption-controlled growth and the influence of stoichiometry on electronic transport in hybrid molecular beam epitaxy-grown BaSnO₃ films. *J. Mater. Chem. C* **5**, 5730–5736 (2017).

35. M. Brahlek, L. Zhang, C. Eaton, H.-T. Zhang, R. Engel-Herbert, Accessing a growth window for $SrVO_3$ thin films. *Appl. Phys. Lett.* **107**, 143108 (2015).

36. J. M. LeBeau, R. Engel-Herbert, B. Jalan, J. Cagnon, P. Moetakef, S. Stemmer, G. B. Stephenson, Stoichiometry optimization of homoepitaxial oxide thin films using x-ray diffraction. *Appl. Phys. Lett.* **95**, 142905 (2009).

37. C. M. Brooks, L. F. Kourkoutis, T. Heeg, J. Schubert, D. A. Muller, D. G. Schlom, Growth of homoepitaxial $SrTiO_3$ thin films by molecular-beam epitaxy. *Appl. Phys. Lett.* **94**, 162905 (2009).

38. O. N. Tufte, P. W. Chapman, Electron mobility in semiconducting strontium titanate. *Phys. Rev.* **155**, 796–802 (1967).

39. Y. Kozuka, Y. Hikita, C. Bell, H. Hwang, Dramatic mobility enhancements in doped $SrTiO_3$ thin films by defect management. *Appl. Phys. Lett.* **97**, 012107 (2010).

40. J. Y. Y. Ayino, T. Wang, B. Jalan, V. Pribiag, Effects of paramagnetic pair-breaking and spin-orbital coupling on multi-band superconductivity. *J. Phys. Condens. Matter.* **32**, 38LT02 (2020).

41. X. Lin, B. Fauqué, K. Behnia, Scalable T^2 resistivity in a small single-component Fermi surface. *Science* **349**, 945–948 (2015).

42. A. Kumar, V. I. Yudson, D. L. Maslov, Quasiparticle and nonquasiparticle transport in doped quantum paraelectrics. *Phys. Rev. Lett.* **126**, 076601 (2021).

43. X. Lin, G. Bridoux, A. Gourgout, G. Seyfarth, S. Krämer, M. Nardone, B. Fauqué, K. Behnia, Critical doping for the onset of a two-band superconducting ground state in $SrTiO_{3-\delta}$. *Phys. Rev. Lett.* **112**, 207002 (2014).

44. E. McCalla, M. N. Gastiasoro, G. Cassuto, R. M. Fernandes, C. Leighton, Low-temperature specific heat of doped $SrTiO_3$: Doping dependence of the effective mass and Kadowaki-Woods scaling violation. *Phys. Rev. Mater.* **3**, 022001 (2019).

45. T. V. Trevisan, M. Schütt, R. M. Fernandes, Impact of disorder on the superconducting transition temperature near a Lifshitz transition. *Phys. Rev. B* **98**, 094514 (2018).

46. A. Joshua, S. Pecker, J. Ruhman, E. Altman, S. Ilani, A universal critical density underlying the physics of electrons at the $LaAlO_3/SrTiO_3$ interface. *Nat. Comm.* **3**, 1129 (2012).

47. H. Fu, K. V. Reich, B. I. Shklovskii, Anomalous conductivity, Hall factor, magnetoresistance, and thermopower of accumulation layer in $SrTiO_3$. *Phys. Rev. B* **94**, 045310 (2016).

48. K. Krishnaswamy, B. Himmetoglu, Y. Kang, A. Janotti, C. G. Van de Walle, First-principles analysis of electron transport in $BaSnO_3$. *Phys. Rev. B* **95**, 205202 (2017).

49. P. Delugas, A. Filippetti, M. J. Verstraete, I. Pallecchi, D. Marré, V. Fiorentini, Doping-induced dimensional crossover and thermopower burst in Nb-doped $SrTiO_3$ superlattices. *Phys. Rev. B* **88**, 045310 (2013).

50. D. V. Christensen, Y. Frenkel, P. Schütz, F. Trier, S. Wissberg, R. Claessen, B. Kalisky, A. Smith, Y. Z. Chen, N. Prydsi, Electron mobility in $\gamma-Al_2O_3/SrTiO_3$. *Phys. Rev. Appl.* **9**, 054004 (2018).

51. F. Lyzwa, Y. G. Pashkevich, P. Marsik, A. Sirenko, A. Chan, B. P. P. Mallett, M. Y.-Rizi, B. Xu, L. M. V.-Arche, D. C. Vaz, G. Herranz, P. Hemme, K. Fursich, M. Minola, B. Keimer, M. Bibes, C. Bernhard, arXiv:2109.06673 (2021).

52. H. Elangovan, M. Barzilay, J. Huang, S. Liu, S. Cohen, Y. Ivry, Engineering individual oxygen vacancies: Domain-wall conductivity and controllable topological solitons. *ACS Nano* **15**, 13380–13388 (2021).

53. E. Mikheev, S. Raghavan, J. Y. Zhang, P. B. Marshall, A. P. Kajdos, L. Balents, S. Stemmer, Carrier density independent scattering rate in $SrTiO_3$-based electron liquids. *Sci. Rep.* **6**, 20865 (2016).

54. D. Van de Marel, J. L. M. van Mechelen, I. I. Mazin, Common fermi-liquid origin of T^2 resistivity and superconductivity in n-type $SrTiO_3$. *Phys. Rev. B* **84**, 205111 (2011).

55. S. Stemmer, S. J. Allen, Non-Fermi liquids in oxide heterostructures. *Rep. Prog. Phys.* **81**, 062502 (2018).

56. X. Lin, C. W. Rischau, L. Buchauer, A. Jaoui, B. Fauqué, K. Behnia, Metallicity without quasi-particles in room-temperature strontium titanate. *npj Quantum Mater.* **2**, 41 (2017).

57. M. W. Swift, C. G. Van de Walle, Conditions for T^2 resistivity from electron-electron scattering. *Eur. Phys. J. B* **90**, 151 (2017).

58. T. A. Cain, A. P. Kajdos, S. Stemmer, La-doped $SrTiO_3$ films with large cryogenic thermoelectric power factors. *Appl. Phys. Lett.* **102**, 182101 (2013).

59. H. W. Jang, A. Kumar, S. Denev, M. D. Biegalski, P. Maksymovych, C. W. Bark, C. T. Nelson, C. M. Folkman, S. H. Baek, N. Balke, C. M. Brooks, D. A. Tenne, D. G. Schlom, L. Q. Chen, X. Q. Pan, S. V. Kalinin, V. Gopalan, C. B. Eom, Ferroelectricity in strain-free $SrTiO_3$ thin films. *Phys. Rev. Lett.* **104**, 197601 (2010).

Anomalous transport in high-mobility superconducting SrTiO₃ thin films

Jin Yue, Yilikal Ayino, Tristan K. Truttmann, Maria N. Gastiasoro, Eylon Persky, Alex Khanukov, Dooyong Lee, Laxman R. Thoutam, Beena Kalisky, Rafael M. Fernandes, Vlad S. Pribiag, and Bharat Jalan

View the article online
https://www.science.org/doi/10.1126/sciadv.abl5668
Permissions
https://www.science.org/help/reprints-and-permissions